

Article

Bismoclite (BiOCl) in the San Francisco de los Andes Bi–Cu–Au Deposit, Argentina. First Occurrence of a Bismuth Oxychloride in a Magmatic–Hydrothermal Breccia Pipe and Its Usefulness as an Indicator Phase in Mineral Exploration

Francisco J. Testa ^{1,2,*}, David R. Cooke ^{1,2}, Lejun Zhang ^{1,2} and Graciela R. Mas ³

¹ CODES-ARC Centre of Excellence in Ore Deposits, Private Bag 79, University of Tasmania, Hobart 7001, Australia; D.Cooke@utas.edu.au (D.R.C.); Lejun.Zhang@utas.edu.au (L.Z.)

² ARC Research Hub for Transforming the Mining Value Chain, Private Bag 79, University of Tasmania, Hobart 7001, Australia

³ INGEOSUR-CONICET, Departamento de Geología, Universidad Nacional del Sur, San Juan 670, Bahía Blanca 8000, Argentina; gmas@criba.edu.ar

* Correspondence: F.J.Testa@utas.edu.au; Tel.: +61-499-988-301

Academic Editor: Maria Economou-Eliopoulos

Received: 29 March 2016; Accepted: 16 June 2016; Published: 28 June 2016

Abstract: The rare bismuth oxychloride, bismoclite (BiOCl), has been identified in the weathered tourmaline–cemented, magmatic–hydrothermal breccia complex at the San Francisco de los Andes Bi–Cu–Au deposit, Argentina. A wide variety of supergene minerals were detected in the oxidized zone, but only preisingerite (Bi₃(AsO₄)₂O(OH)) is intimately associated with bismoclite. Bismuth arsenate is present either as minor accessory phases or as traces in bismoclite-rich samples. This is the first documented occurrence of bismoclite in a porphyry-related, and magmatic–hydrothermal breccia pipe deposit. Bismoclite is interpreted to have formed by weathering of hypogene bismuthinite (Bi₂S₃), which originally occurred with arsenopyrite to cement the breccias. These appear to have reacted with O₂- and HCl-bearing meteoric waters to produce pockets of supergene bismoclite–preisingerite assemblages. Bismoclite samples have been characterized by means of X-ray diffractometry (XRD), geochemistry, petrography, scanning electron microscopy (SEM), differential thermal analysis–thermogravimetry analysis (DTA–TGA) and infrared analysis (IR) providing useful insights and updated information regarding this rare bismuth oxychloride and associated arsenate mineral. The San Francisco de los Andes breccia complex shows similar geometry, morphology and internal organization as those found in traditional magmatic–hydrothermal breccias associated with Cu–Mo porphyry deposits. Bismoclite and preisingerite form due to the presence of hypogene Bi-bearing minerals followed by appropriate supergene conditions. These hypogene minerals commonly occur only as trace phases, or are entirely absent, in porphyry and related magmatic–hydrothermal breccia deposits. The scarcity of hypogene Bi–mineral phases in porphyry and related magmatic–hydrothermal breccia deposits is the main reason why bismoclite has not previously been reported in these types of deposits. The detection of bismoclite as a mineral phase in the oxidized zone of weathered deposits highlights hypogene Bi mineralization at depth, and associated metals. Bismoclite is an insoluble mineral of particular interest in those supergene profiles which have been completely leached out of distinctive, water-soluble phases, such as Cu sulfate minerals, which are diagnostic of Cu mineralization at depth. Consequently, bismoclite could potentially be the only indicator of hypogene and supergene mineralization in lower portions of a bismuth bearing ore deposit.

Keywords: bismoclite; magmatic–hydrothermal breccia pipe; porphyry-related; San Francisco de los Andes; Argentina

1. Introduction

This article reports the occurrence of bismoclite (BiOCl) within the weathering zone of the San Francisco de los Andes deposit. This rare bismuth oxyhalide occurs as whitish, dusty and soft pockets in oxidized, cement-supported breccias and it is typically associated with preisingerite ($\text{Bi}_3(\text{AsO}_4)_2\text{O}(\text{OH})$). The first description of bismoclite was by Mountain (1935) [1] from a yellowish and greenish specimen of eluvial origin collected on the surface of a pegmatite outcrop at Steinkopf, Namaqualand, Cape Province of South Africa. Preisingerite, an equally rare bismuth arsenate, was first described by Bedlivy and Mereiter (1982) [2] at the San Francisco de los Andes Bi–Cu–Au deposit, Argentina, which is the type locality for this mineral. They found preisingerite occurring as poorly developed small translucent greyish white crystals within the weathered zone.

Since bismoclite’s initial discovery and description, it has been identified in only a few localities around the world, mainly as alluvial specimens near bismuth-bearing granite pegmatites, or as weathering products of bismuth sulfides in greisen-related deposits. This study documents the first occurrence of bismoclite in a magmatic–hydrothermal breccia complex, and porphyry-related deposit.

Table 1 summarizes the different geological environments where bismoclite has previously been reported. Although the most common occurrences are associated with pegmatitic or greisen mineralization, it has also been documented, among others, in low- and high-sulfidation epithermal and volcanic-hosted massive sulfide deposits.

Table 1. Global occurrences of bismoclite, subdivided by deposit type.

Ore Deposit Types	Occurrences	References
Pegmatite	Alto do Giz, Rio Grande do Norte, Brazil	[3]
	Alto Feio, Paraíba, Brazil	[4]
	Barra do Corda, Bahia, Brazil	[3]
	Cala Francese Quarries, Sardinia, Italy	[5]
	Heftejern, Telemark, Norway	[6]
	Jackals Water, Namaqualand, South Africa	[1]
	Mt Holland, Western Australia, Australia	[7]
	Old 25 Pipe, Kingsgate, New South Wales, Australia	[8]
	Rubikon Mine, Erongo Region, Namibia	[9]
	Tennvatn, Nodland, Norway	[10]
Greisen-related	Bygoo, New South Wales, Australia	[11]
	Kara-Oba W deposit, Karagandy Province, Kazakhstan	[12]
	Wittichen, Black Forest, Baden-Württemberg, Germany	[13]
W–Mo–(Bi) quartz veins	Wolfram Mine, Victoria Australia	[14]
Ancient high-sulfidation systems: epithermal deposit	The Diablillos, Salta, Argentina	[15]
	Goldfield, Nevada, USA	[16]
Active high-sulfidation systems: fumaroles in geothermal fields	El Guanaco Mine, Antofagasta Region, Chile	Private collection
	Kudriavvy Volcano, Far–Eastern Region, Russia	[17]
	La Fossa Crater, Sicily, Italy	[18]
Low-, and intermediate-sulfidation epithermal deposits	Mutnovsky volcano, Far–Eastern Region, Russia	[19]
	Round Mountain District, Nevada, USA	[20]
	Tary-Ekan, Karamazan Mts, Tajikistan	[7]
Sn–Ag polymetallic veins	Falcacci mine, Rio Marina, Tuscany, Italy	[21,22]
	Tazna, Potosi Department, Bolivia	[23]
Metasediment-hosted polymetallic veins	Croft Gothel Mine, Cornwall, England	[24]
Metamorphic-hosted orogenic deposit	Reward Mine, California, USA	[25]
Carbonate-hosted Au–Pb–Zn replacement deposit	Tintic District, Utah, USA	[11,26]

Table 1. Cont.

Ore Deposit Types	Occurrences	References
Quartzite-hosted, high-grade Cu replacement deposit	Ashio mine, Honshu Island, Japan	[27]
Volcanogenic massive sulfide deposits	Escanaba Trough, East Pacific Rise, Pacific Ocean	[28]
Banded iron formation	Iron Monarch open cut, Southern Australia, Australia	[29]
Orthomagmatic Ni–Cu–Fe deposit	Strathcona deposit, Sudbury district, Ontario, Canada	[30]

Although bismoclite occurs naturally in weathered ore deposits, it is rare and not economical to mine. It can be produced as a byproduct from refining Pb and Cu ores by combining Bi with Cl and O. The synthesis of bismuth oxychloride is most effectively carried out by chlorination of raw bismuth ($2\text{Bi} + \text{Cl}_2 = 2\text{BiCl}_3$) with subsequent hydrolysis of the resulting bismuth trichloride ($\text{BiCl}_3 + \text{H}_2\text{O} = \text{BiOCl} + 2\text{HCl}$; [31]). Another possibility to synthesize bismuth oxychloride is by adding hydrochloric acid and sodium hydroxide in a bismuth nitrate solution at a constant pH and temperature [32].

Bismuth oxychloride has been used for several decades as a pigment. It was the first feasible synthetic pearlescent pigment developed over 50 years ago [33]. The two main modern commercial forms of pearlescent pigments are bismuth oxychloride and titanium dioxide (or ferric oxide) coating on micas [32,34]. The highest quality synthetic BiOCl-based pearlescent pigment occur as 11 to 15 μm sized hexagonal-shaped platelets due to their narrow particle size, high refractive index and flat shape. Bismuth oxychloride has a smoother surface and approximately twice the reflectance of the best titanium dioxide mica-based alternatives, and similar reflectivity to aluminum [32,34,35].

Bismoclite is used for coating metal, plastic, paper, leather and even wood to sharply bring out features in furniture [32,34,35]. Bismuth oxyhalide has been used in cosmetics since ancient Egypt, and has been used widely in recent years in various beauty care products, mainly makeups as it has a silky feel, good slip, good adhesion and an iridescent effect that helps to conceal skin imperfections due to its light reflecting property [34,35]. Bismoclite can also give a metallic appearance to certain non-metallic materials and it is the most common coating used to make simulated pearls [32,35]. Bismuth oxychloride has also been used as a key ingredient in certain inks and paints to replace the metallic formulation that may have environmental concerns [32].

2. Geology

The San Francisco de los Andes mine is located at $30^\circ 50' 08''$ S latitude and $69^\circ 35' 58''$ W longitude, on the eastern flank of the Frontal Cordillera, San Juan Province, Argentina (Figure 1). The Frontal Cordillera is a geological province on the eastern flank of the Cordillera de los Andes. It currently extends from northern San Juan Province to southern Mendoza Province, and it used to be part of the western margin of Gondwana. The San Francisco de los Andes mine is the most important ore deposit within the Bi–Cu–Au San Francisco de los Andes district, which extends 30 km north along the Frontal Cordillera [36].

The San Francisco de los Andes orebody is hosted by a tourmaline–quartz–cemented breccia pipe that cuts sedimentary rocks of Carboniferous age [37]. The Agua Negra Formation is characterized by marine sandstones, shales and siltstones that strike north with a steep dip to the east (Figure 1). This formation can be divided in two tectonostratigraphic units: (1) a Carboniferous to Lower Permian pre-orogenic sequence, which formed when the Frontal Cordillera occupied a backarc position, with east to west propagation of a deltaic system to open marine conditions [38–40]; and (2) a Permian syn-orogenic marine sedimentary sequence that developed when the Frontal Cordillera had a tectonic setting consistent with a retroarc foreland basin, with a western provenance due to the uplift of the volcanic arc [39,40].

The sedimentary rocks are intruded by the Tocota Pluton, a Permian intrusive complex that compositionally ranges from tonalite to granite [41]. Close to San Francisco de los Andes mine, the

Tocota Pluton has been divided into two main units: (1) Amancay; and (2) Chorrillos (Figure 1). The Tocota Pluton defines the southernmost edge of the Colangüil Batholith, a group of intrusions emplaced along the margin of Gondwana, which extend along the Frontal Cordillera from central to north San Juan Province.

During the Carboniferous, after the collision of the Chilena terrane, a magmatic arc formed along the western margin of Gondwana due to subduction of a proto-Pacific oceanic plate [42–45]. The early intrusions of the Colangüil Batholith were emplaced in a volcanic arc setting, whereas the later intrusions formed in an extensional, post-orogenic regime, immediately before the rifting of Gondwana [45,46].

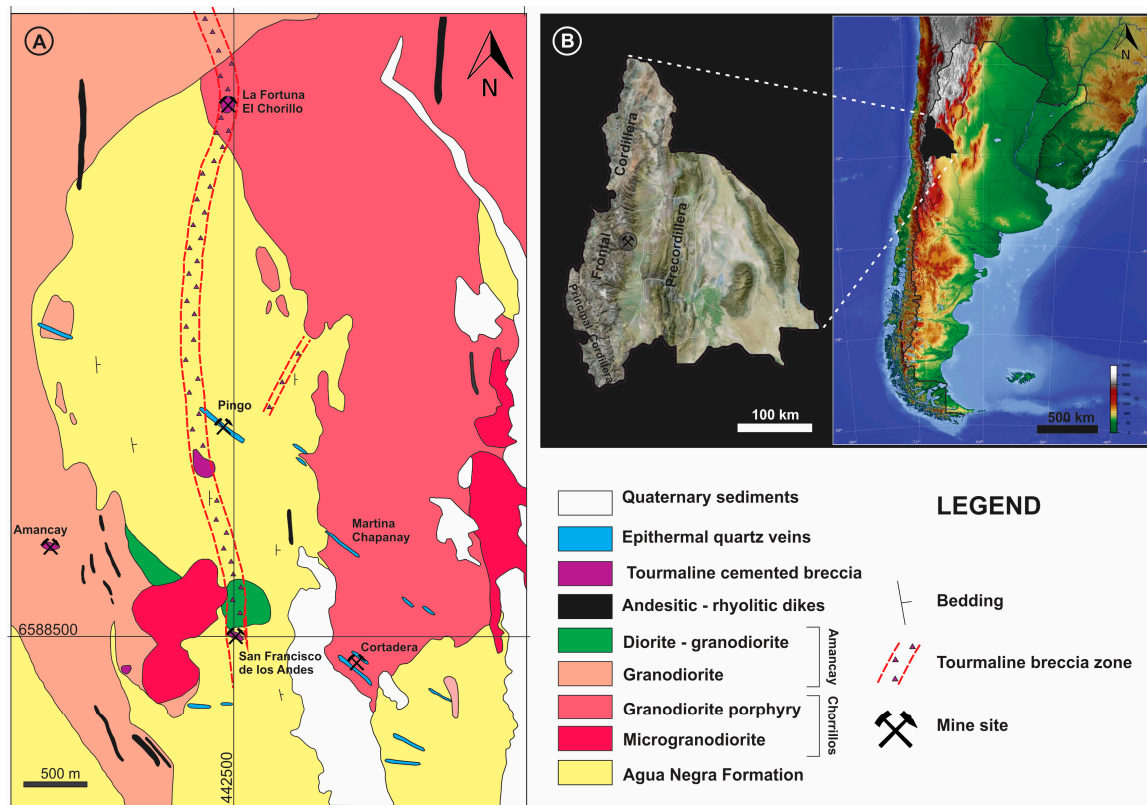


Figure 1. (A) Geological maps of the southern area of the San Francisco de los Andes district (modified after Llambías and Malvicini, 1969 [37]). (B) Location of Frontal Cordillera and San Francisco de los Andes mine in San Juan Province (left); and San Juan's location in Argentina (right).

The San Francisco de los Andes Breccia Complex

The San Francisco de los Andes tourmaline–cemented breccia complex has an elongated NW-trending elliptical shape with a constriction in the middle. Based on underground work, the ‘figure eight’ shape divides the breccia complex into a NW and a SE domain that can be traced up to 75 meters below surface (Figure 2). With increasing depth, the geometry of the breccia complex resembles two roughly cylindrical breccia bodies with shared edges, rather than one single elliptical body (Figure 2). This geometry, along with the progressive upward narrowing and ‘necking’ of the structure, are consistent with the upper levels of eroded magmatic–hydrothermal breccia pipes. The idea of a deep mineralized tourmaline–quartz–cemented breccia column (>170 m) is in agreement with the fact that drill holes have not reach the root of the orebody (Figure 2B).

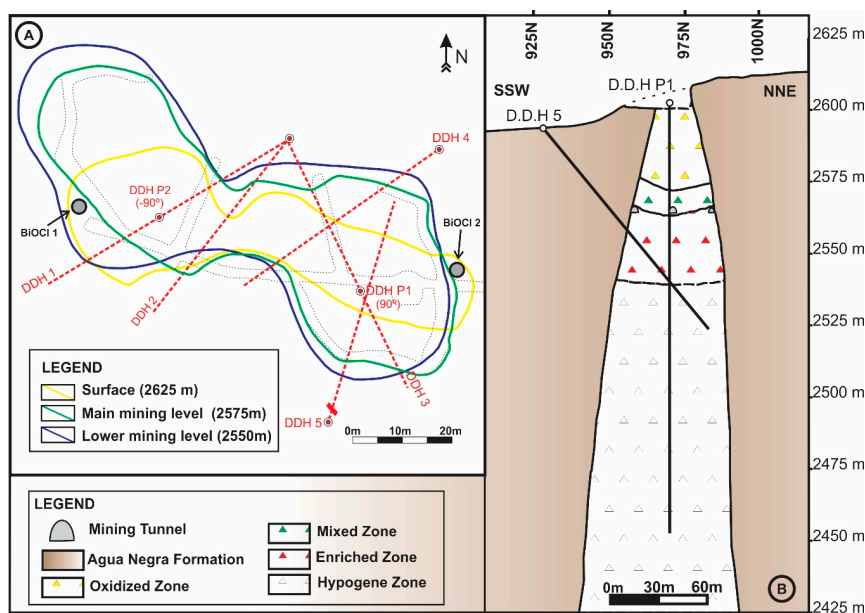


Figure 2. (A) Outline of San Francisco de los Andes breccia body as a function of depth (three horizontal sections). Note the location of the two representative bismoclite samples collected from the surface. (B) SSW–NNE cross section of the breccia pipe describing the vertical zonation of the supergene profile, with its three distinct horizons: oxidized, mixed and enriched zone (modified after Lencinas (1990) [47]).

The San Francisco de los Andes deposit hosts the largest bismuth concentration in a breccia body in Argentina [36]. The orebody is characterized by a complex Bi–Cu–Au–As–Fe–Zn–Pb–Ag mineral assemblage, including sulfides, sulfosalts and native elements, as well as supergene arsenates, sulfates, carbonates, oxides and hydroxides (Table 2). The deposit was mined sporadically between the 1940s and the 1980s. A total of 112 tons of bismuth concentrate was produced, and 2420 tons of ore with 3%–6% Cu and 1.2%–4.5% Bi [36,48]. In 1990, Aguilar Mining Company estimated a resource of >0.16 Mt with 5.4 g/t Au, 77 g/t Ag, 0.9% Cu, 0.15% Bi, 0.4% Pb and 0.1% Zn for the 35 m thick ‘enriched zone’. Although the vertical extent of the breccia pipe is unknown, they identified a shallow (20–25 m) hypogene zone comprising sulfide and sulfosalt minerals with average grades of 1.32 g/t Au, 65.5 g/t Ag, 0.55% Cu, 0.02% Bi, 0.38% Pb and 0.61% Zn [47].

The hypogene zone is located 70 m below the surface and is open at depth (Figure 2). The magmatic–hydrothermal breccia complex has been divided into rim and core facies, based on its proximity to the contact with the sedimentary host rock. Rim facies are characterized by very angular to angular tabular sedimentary clasts, which are parallel and vertical to steeply dipping inwards. These breccias are rich in hypogene hydrothermal cement including silicates (tourmaline ± quartz) and ore minerals comprising sulfides and sulfosalts (Table 2). Vugs are generally not common, except in specific areas where they are the characteristic feature of the breccia facies. Matrix is absent or very minor. The internal organization of the rim facies varies from jigsaw-fit to clast-rotated, stratified and ungraded. The rim facies can be subdivided into six sub-facies based on their distinctive, and/or most abundant, infill: (1) tourmaline–quartz–cemented; (2) arsenopyrite–cemented; (3) bismuthinite–cosalite–chalcocopyrite–cemented; (4) galena–cemented; (5) sphalerite–cemented; and (6) vug–rich breccias. Additional minor and trace minerals occur as hydrothermal cement in each sub-facies (Table 2).

The core facies has sub-angular to sub-rounded sedimentary clasts randomly oriented. This facies is matrix- and vug-rich with considerably less hypogene hydrothermal cement than is present in the rim facies. Silicates forming cement (tourmaline ± quartz) are more abundant than sulfides and sulfosalts (Table 2). The core facies breccias is clast-rotated to chaotic, poorly stratified and ungraded to massive.

Table 2. Hypogene and supergene minerals identified at San Francisco de los Andes. Mineral types were confirmed by X-ray diffraction (Testa, 2016; unpublished data). The relative proportion of each mineral is expressed as: abundant (**bold**), minor (not bold), and trace concentrations (in brackets). The characteristic metals and metalloids for those less common minerals are listed between square brackets.

Sulfides	Sulfosalts	Native Elements	Arsenates	Sulfates	Carbonates	Oxides and Hydroxides	Silicates
bismuthinite	cosalite [Pb–Bi]	(Au)	scorodite	chalcantite [Cu]	(bismutite) [Bi]	goethite	tourmaline
arsenopyrite	(emphlectite) [Cu–Bi]	(Bi)	preisingerite [Bi]	(brochantite) [Cu]	(siderite)	lepidocrocite	quartz
chalcopyrite	(cuprobismutite) [Cu–Bi]		rooseveltite [Bi]	(anglesite)	(malachite)	hematite	(chrysocolla)
galena	(tetrahedrite) [Cu–Fe–Sb]		beudantite [Pb–Fe]	(jarosite)	(azurite)	(cassiterite)	
sphalerite	(luzonite) [Cu–As]		olivenite [Cu]	(alunogen) [Al]	(calcite)	(cuprite)	
pyrite			conichalcite [Ca–Cu]	(gunningite) [Zn–Mn]		(tenorite)	
bornite			(clinoclase) [Cu]	(starkeyite) [Mg]			
chalcocite			(mixite) [Bi–Cu]	(hexahydrite) [Mg]			
covellite			(rollandite) [Cu]	(anhydrite)			
digenite				(gypsum)			
(molybdenite)							
(stibnite)							

Supergene processes have intensely modified the hypogene assemblages to produce complex secondary assemblages. Oxides, hydroxides, arsenates, sulfates and carbonates formed contemporaneously across the San Francisco de los Andes breccia pipe’s weathering profile (Figure 2). The study area has a desert climate with little precipitation. The low average rainfall prevented the development of distinctive zones within the supergene profiles. There is no gossan cap, and the deposit lacks a well-defined leached zone. Instead, a rough vertical zonation of supergene minerals has been identified. Here, arsenates and Fe oxides-hydroxides are preferentially concentrated close to the surface, whereas the more mobile sulfates and carbonates were identified both at surface and in the underground mine levels, and particularly along the more permeable rims of the breccia pipe. Two supergene zones with distinctive mineralogies are defined here: (1) oxidized; and (2) enriched. The presence of a <10 meter transitional zone is defined here as the mixed zone, which contains characteristic minerals from both the oxidized and enriched zones (Figure 2).

The oxidized zone constitutes the upper part of the deposit, a <40 m thick horizon. Hematite, goethite and lepidocrocite are common insoluble oxidized minerals found near the surface but their abundance is not high enough to form a true gossan. The most common minerals in the oxidized zone are arsenates. Bedlivy and Llambias (1969) [49] documented Cu, Fe and Pb arsenates from the weathering profiles of the San Francisco de los Andes deposit. The most abundant arsenate species is scorodite, commonly associated with Fe oxides–hydroxides and locally with rare Fe–Pb arsenate–sulfate (beudantite). Rooseveltite (BiAsO₄) and preisingerite (Bi₃(AsO₄)₂O(OH)) are the most common Bi arsenate in the oxidized zone. Both are locally accompanied by the less abundant Bi–Cu arsenate (mixite) and Bi carbonate (bismutite). Preisingerite is intimately associated with bismoclite pockets and are commonly intergrown. The most common Cu arsenates are olivenite (Cu₂AsO₄(OH)) and conichalcite (CaCu(AsO₄)(OH)), which are intimately associated with one another. Clinoclase (Cu₃(AsO₄)(OH)₃) is common but less abundant than olivenite and conichalcite, and not only restricted to the surface outcrops, but also to deeper levels. It is commonly associated with Cu sulfates and rarely with olivenite and conichalcite.

Sulfates are the second most abundant group of supergene minerals after arsenates. In contrast to the more immobile Cu arsenates, Cu sulfates are not only restricted to the surface outcrops, but also occur in the oxidized and mixed zones (Figure 2). Chalcanthite ($\text{CuSO}_4 \cdot 5(\text{H}_2\text{O})$) is a major weathering product that occurs at surface, along the weathering profile, and as a precipitate covering the roof and walls of underground tunnels. Where present, brochantite ($\text{Cu}_4\text{SO}_4(\text{OH})_6$) is intimately associated with chalcanthite though it is less abundant. Anglesite (PbSO_4) is very rare and was only detected in surface outcrops as irregular crusts surrounding relict galena. Gypsum is a minor, but ubiquitous, sulfate. Carbonates are rare; malachite and azurite are scarce and only occur associated with Cu sulfates and minor chrysocolla, whereas siderite and calcite are uncommon (Table 2).

The enriched zone occurs below the oxidized zone. This forms a <35 m thick high-grade horizon where secondary sulfosalts and sulfides are abundant. Luzonite, covellite and chalcocite formed slightly after the mineral assemblages that characterize the oxidized and mixed zones (i.e., oxides, arsenates, sulfates and carbonates). Weakly weathered arsenopyrite–chalcopyrite samples commonly exhibit botryoidal luzonite veins along the contact between arsenopyrite and chalcopyrite. Replacement rims composed of chalcocite, digenite and covellite surrounding chalcopyrite commonly are developed in contact with luzonite. Original hypogene chalcopyrite, and in some cases bornite, has been replaced by chalcocite and covellite. These grade from thin rims to pervasive replacements with barely noticeable relicts of chalcopyrite and/or bornite. Luzonite and secondary Cu sulfides also occur as colloform veinlets that cut the hypogene assemblages. Both secondary sulfosalts and sulfides are common in the supergene enriched and mixed zones.

Several neof ormation post–mining coatings of efflorescent sulfate minerals were identified in the underground workings. Alunogen ($\text{Al}_2(\text{SO}_4)_3 \cdot 17(\text{H}_2\text{O})$) evenly occurs along the walls and roof of underground tunnels and is commonly associated to chalcanthite. Gunningite ($\text{Zn}_{0.75}\text{Mn}^{2+}_{0.25}(\text{SO}_4) \cdot (\text{H}_2\text{O})$) is less abundant and locally occurs coating those walls where sphalerite is present. Starkeyite ($\text{MgSO}_4 \cdot 4(\text{H}_2\text{O})$) is the least common efflorescent sulfate but can still be found associated with sulfide bearing underground workings. Hexahydrate ($\text{MgSO}_4 \cdot 6(\text{H}_2\text{O})$) was identified as traces to major admixtures with starkeyite. Traces of gypsum ($\text{CaSO}_4 \cdot 2(\text{H}_2\text{O})$) also occur associated with both magnesium sulfates.

3. Methodology

3.1. Sample Collection

Bismoclite–preisingerite bearing breccia samples were collected from the surface of the oxidized zone at San Francisco de los Andes. Most of the specimens collected had only small clusters or patches of bismoclite (confirmed by means of X-ray diffraction). Two representative samples were selected for further analyses (Figure 2). These were the only two samples with large enough oxyhalide pockets to be chemically analyzed, which ranged in size from 2 to 3 cm³.

3.2. X-Ray Diffraction Analytical Methods

Powder X-ray diffraction (XRD) analyses were conducted at the Geology Department, Universidad Nacional del Sur, on a Rigaku D–Max III–C automatic powder diffractometer (Rigaku, Tokyo, Japan) with Cu K α radiation and graphite monochromator to remove the K α_2 contribution. Each analysis was performed using an accelerating voltage of 30 kV and an electric current of 15 mA. The powder XRD data were obtained over a 2 θ diffraction angle range of 3° to 60°, with a 0.024° step size and 1 s per step counting time.

The bismoclite unit cell parameters were calculated and refined with MDI jade 7 software (Materials Data Incorporated, Livermore, CA, USA). The crystallite size for each basal reflection was calculated from (001), (002) and (003) line profiles using the same software package. Bismoclite diffraction data were fitted with a pseudo–Voigt curve profile shape function. The former represent a linear combination of Gaussian and Lorentzian components, whereas a true Voigt curve is a convolution of the Gaussian and Lorentzian components.

3.3. Geochemistry Methods

Selected bismoclite–preisingerite samples were powdered with an agate mortar, washed carefully in distilled water and air dried at room temperature. Only handpicked homogeneous material was collected, with no evident tourmaline needles, arsenopyrite or iron hydroxides/arsenates.

Powdered samples were analyzed at Actlabs (Activation Laboratories, Ancaster, ON, Canada) using litho-geochemical methods (group 4 packages) including both 4F–Cl–INAA and 4F–H₂O^{+/-}–gravimetric packages. Eight sodium peroxide fusion ICPMS package determined the Bi and As proportions. Several reference materials were used for quality control, which include GXR-1, GXR-4, MAG-1 (depleted), NIST 1632c, MP-2, ZW-C, NCS DC70014 and MP-1b.

3.4. Microscopy Methods

A Nikon E600 POL binocular petrographic microscope (Nikon, Tokyo, Japan) with $\times 5$, $\times 10$, $\times 20$ and $\times 50$ objective lenses as well as $\times 10$ ocular lenses was used to carry out the petrographic studies. Scanning electron microscopy (SEM) studies were conducted at Centro Científico Tecnológico (UAT–CCTBB), Bahía Blanca, Argentina. A LEO EVO 40 XVP scanning electron microscope (Zeiss, Oberkochen, Germany) using an acceleration voltage of 15 kV and a beam current between 1 and 0.5 nA was used to analyze 11 gold-coated bismuth oxychloride samples.

3.5. Thermal Analytical Methods: Differential Thermal Analysis and Thermogravimetry Analysis (DTA–TGA)

Thermal experiments were carried out at Centro de Tecnología de Recursos Minerales y Cerámica (CETMIC), La Plata, Argentina. Three curves were obtained using a NETZSCH Simultaneous Thermal Analysis Apparatus STA 409/C (Netzsch Group, Selb, Germany) at a heating rate of 10 °C/min. Measurements were obtained up to 1050 °C using a 124 mg sample in an Al₂O₃ crucible in an air atmosphere using α -alumina reference material.

3.6. Infrared Analytical Methods

Infrared analyses were conducted at the Chemistry Department, Universidad Nacional del Sur, Bahía Blanca, Argentina. Infrared spectra were obtained by means of Fourier Transform Infrared Spectroscopy (FTIR) using a Nicolet–Nexus 470 FT–IR spectrometer (Thermo Scientific, Waltham, MA, USA) with a Nichrome source detector and KBr beamsplitter. Data acquisition was carried out against a KBr background, with a total of 32 scans within the wavelength range that corresponds to the mid-infrared spectrum (4000–400 cm⁻¹). The six samples were prepared as solid–solid dispersion with 1.5 mg of dry material in 150 mg of anhydrous KBr. The size of the resulting tablets was 10 mm in diameter and 2 mm thick.

4. Results

4.1. X-Ray Diffraction Analyses and Crystal Structure Study

Over 30 powder X-ray diffraction analyses were carried out on carefully selected bismoclite samples aiming to avoid impurities such as tourmaline needles, as well as Fe oxides and hydroxides. Every analysis exhibited strong reflections at low 2θ angle in comparison to the standard non-oriented sample (e.g., Figure 3). Such behavior is explained due to a preferred orientation parallel to the perfect cleavage along (001) planes, which correspond to the first spike recorded. Note the intensity of the second and the seventh reflection, which represent the (002) and (003) planes, are also strongly enhanced as a result of preferred orientation along the cleavage surface (Figure 3A).

The bismoclite unit cell parameters were calculated and refined: the bismuth oxychloride crystals correspond to a primitive tetragonal crystal system, where the a and b axes lengths are 3.891 Å (standard deviation: 0.031 Å) and the c axis extension is 7.374 Å (standard deviation: 0.004 Å). After precise lattice constants were determined, the resulting unit volume is 111.673 Å³.

The crystallite size for each basal reflection was calculated from (001), (002) and (003) line profiles. Since bismoclite is a supergene phase at San Francisco de los Andes, and therefore free of lattice strain, the average crystallite size could be estimated according to the Scherrer formula as follows:

$$\text{Mean Crystallite Size} = K \cdot \lambda / (\text{FWHM} \cos\theta)$$

- K is a dimensionless shape factor that varies with the actual crystallite shape, but it is commonly 0.9.
- λ is the X-ray wavelength.
- FWHM (Full Width at Half Maximum) is the specimen broadening of any single peak at half the maximum intensity in radians.
- θ is the Bragg angle.

Table 3 lists the calculated mean crystallite thickness (t) for the three basal planes within the 3° – 60° X-ray scan as well as its fitting error (e), the t/d ratio and the number of planes per crystalline domain.

Table 3. Estimated crystallite size and related parameters for bismoclite from San Francisco de los Andes.

hkl	2 θ (deg)	d (Å)	t (nm)	e (nm)	t/d	n
(001)	12.071	7.3262	29	2	3.94	3.94/1 \approx 4
(002)	24.167	3.6797	34	2	8.15	8.15/2 \approx 4
(003)	36.528	2.4579	28	2	12.24	12.24/3 \approx 4

Preisingerite was always present in our XRD analyses to some extent. It occurs either as a trace mineral with very weak reflections (Figure 3A), or as an associated phase with clear reflections, although they are never as strong as bismoclite (Figure 3B). The four most intense reflections for preisingerite are grouped between 2θ value of 27° and 30° . Only traces of preisingerite are present in the sample shown in Figure 3A, where these four most intense reflections are barely detectable.

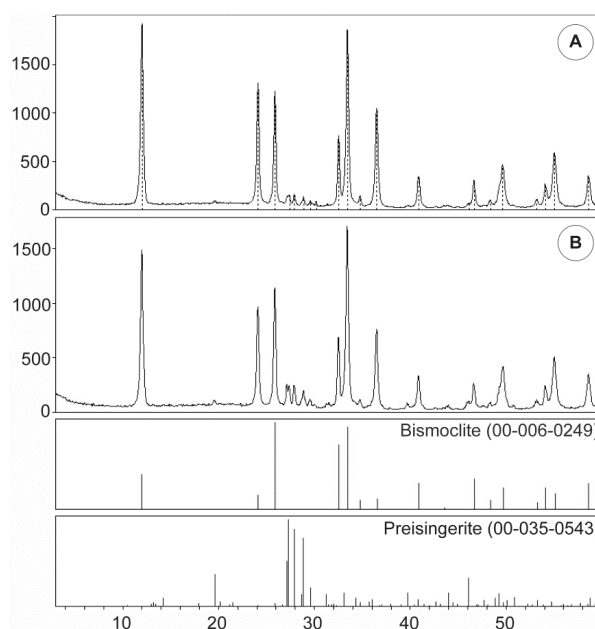


Figure 3. Bismoclite's oriented X-ray diffractograms (above) and reference non-oriented reflection data (below). (A) Bismoclite with traces of preisingerite. Note that the first reflection corresponding to (001) plane, is 2.5 times more intense than the 00-006-0249 reference data. In a similar manner, the intensity of the second reflection (002), as well as the seventh peak (003), are 3.9 and 3.2 times stronger, respectively, than the reference pattern. (B) Bismoclite with minor preisingerite. Note the four most intense reflections of preisingerite grouped between 27° and 30° .

4.2. Geochemistry Results

Figure 4 shows one of the bismoclite pockets analyzed. Note the pure bismoclite core and preisingerite–tourmaline rich rims. The dark reddish-brown material represents sedimentary clasts partially altered to hematite, goethite and scorodite.

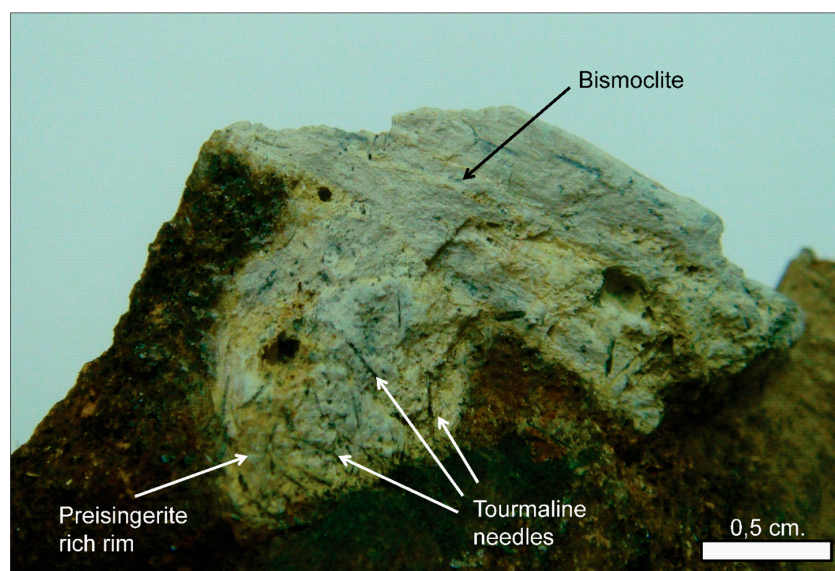


Figure 4. Bismoclite cluster with preisingerite and tourmaline needles near the margins. Sample: 05–BiOCl–02, San Francisco de los Andes.

The ideal chemical compositions for bismoclite (BiOCl) and preisingerite ($\text{Bi}_3(\text{AsO}_4)_2\text{O}(\text{OH})$) are listed in Table 4. The chemical results provided by Actlabs Ltd (Ancaster, ON, Canada) are shown in Table 5. From these, it was possible to estimate the proportions of the mineral phases. For the first sample, less than 2/3 of the bismuth corresponds to bismoclite and 1/3 to preisingerite and relict bismuthinite, whereas for the second sample more than 2/3 represents Bi oxyhalide and less than 1/3 Bi-bearing arsenide and sulfide. The excess in Bi has been attributed to relict bismuthinite.

Table 4. Ideal chemical composition for bismoclite and preisingerite reported in weight %.

Species	Bi	Cl	O	H	As	Total
Bismoclite	80.24	13.61	6.14	-	-	99.99
Preisingerite	66.85	-	17.06	0.11	15.98	100.00

Table 5. Chemical results provided by Actlabs Ltd for bismoclite–preisingerite bearing samples from San Francisco de los Andes.

Analyte	Cl (wt %)	Mass (g)	H_2O^+ (wt %)	H_2O^- (wt %)	Bi (ppm)	As (ppm)
Detection Limit	0.01	-	0.1	0.1	2	5
Method	INAA	INAA	GRAV	GRAV	FUS–MS– Na_2O_2	FUS–MS– Na_2O_2
BiOCl 01	8.38	1.024	0.8	0.3	711,000	20,300
BiOCl 02	9.36	1.037	0.2	0.3	731,000	15,000

4.3. Microscopy Results

In thin section, bismoclite aggregates are colorless, have very high surface relief and extremely high birefringence. Even though bismoclite belongs to the uniaxial negative optical class [7], this could not be determined as there were no appropriate crystals to obtain a clear interference figure.

Based on the SEM study, the most common form of bismoclite identified at San Francisco de los Andes occur as small platy crystals (Figure 5). Well oriented aggregates were dominant, although randomly oriented aggregate patches were also present. Rosette-like habits were locally documented and rare rectangular prisms with truncated corners could also be distinguished (Figure 5).

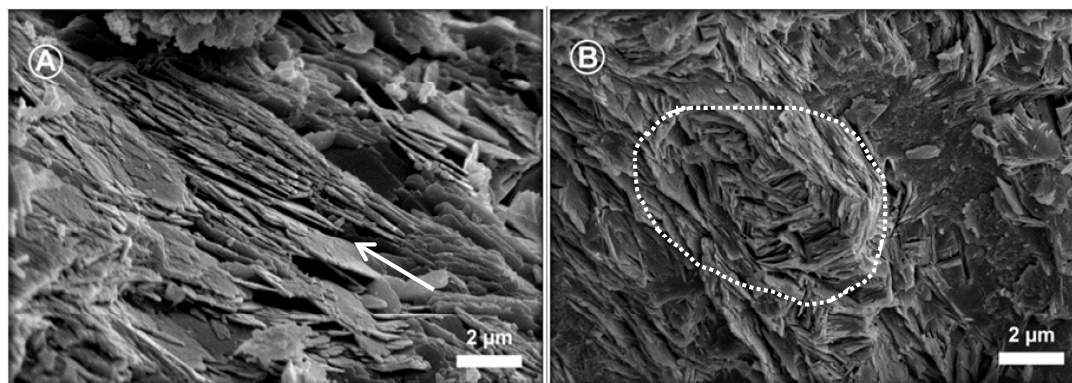


Figure 5. Two distinctive morphologies of bismoclite from San Francisco de los Andes seen under SEM (Sample 05–BiOCI–02): (A) Platy bismoclite crystals. Note the well-developed cleavage parallel to the (001) plane (white arrow). (B) A rosette-like bismoclite aggregate is shown in the white dotted line.

4.4. Thermal Analyses Results: DTA and TGA

The thermal analyses showed a mass loss of 1.1% between 20 and 450 °C along with an exothermic break in the DTA curve. Between 450° and 1000 °C, a mass loss of 21.7% was recorded, together with a double endothermic spike with maximum values at 865 and 893 °C (Figure 6).

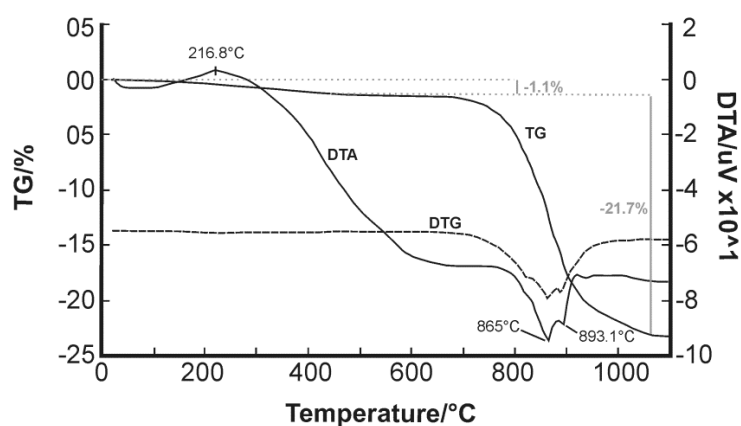


Figure 6. Characteristic DTA, TG and DTG curves for bismoclite–preisingerite pockets from San Francisco de los Andes (Sample: 05–BiOCI–02).

4.5. Infrared Analyses Results

Six samples were analyzed by means of FTIR spectroscopy. A representative spectrum from San Francisco de los Andes is shown in Figure 7. Four main sharp absorption bands were recorded at $<1700\text{ cm}^{-1}$, along with the beginning of an absorption band at 470 cm^{-1} . The latter was only partially documented due to equipment limitations. Additional minor inflexions (i.e., single and double shoulders) were recorded within the same portion of the electromagnetic spectrum ($1700\text{--}470\text{ cm}^{-1}$; Figure 7). A strong and wide absorption band was documented at wavelengths between 4000 and 1700 cm^{-1} (Figure 7).

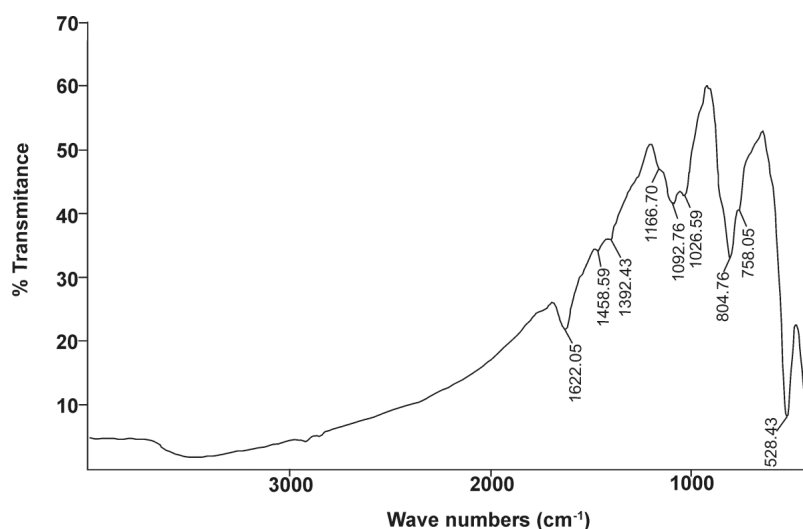


Figure 7. Characteristic Infrared spectrum for bismoclite–preisingerite pockets from San Francisco de los Andes (Sample: 05–BiOCl–02).

5. Discussion

5.1. Comparison of Analytical Results

The crystal structure of bismoclite and other bismuth oxyhalides has only been studied by a few authors. Major contributions were made by Bannister and Hey (1934, 1935) [50,51] who carried out structural research by photographic methods. The bismuth oxychloride structure was described in detail by Keramidis et al. (1993) [52], who synthesized bismoclite plates, selected a small single crystal, centered it on a single crystal diffractometer and then refined the cell constants by a least-squares procedure. Table 6 summarizes the unit cell dimensions and crystal structure parameters for synthetic and naturally occurring bismoclite, and highlights the consistency between previous studies and our XRD results. Ketterer and Krämer (1986) [53] documented and refined the structure of bismuth oxybromide, a compound analogous to bismuth oxychloride that is a member of the bismuth oxyhalide family.

Table 6 also lists the calculated crystallite size yielded for bismoclite from San Francisco de los Andes. As the 2θ angle increases, the instrumental error decreases, thus the crystallite size obtained for the (003) reflection is more reliable than for (001) and even (002). In addition to crystallite size, a diversity of factors can contribute to the diffraction peak widening. The most significant factors include inhomogeneous strain and instrumental effects [54]. The Scherrer equation only provides a lower limit on the particle size, therefore a larger crystallite size than its actual dimensions may be obtained as a result of a non-zero contribution.

Table 6. Unit cell dimensions and axial ratio for naturally occurring and synthetic bismoclite. The crystallite thickness calculated for the three basal planes for bismoclite from San Francisco de los Andes is also listed.

Bismoclite Type [source]	Unit Cell Dimensions		Axial Ratio	Crystallite Thickness (nm)		
	a & b (Å)	c (Å)				
Synthetic BiOCl [51]	3.89 ± 0.01	7.37 ± 0.02	1:1.895	-	-	-
Naturally occurring BiOCl [1,51]	3.89 ± 0.01	7.37 ± 0.02	1:1.895	-	-	-
Synthetic BiOCl [52]	3.887	7.354	1:1.892	-	-	-
San Francisco de Los Andes	3.891 ± 0.031	7.374 ± 0.004	1:1.897	29 ± 2 (001)	34 ± 2 (002)	28 ± 2 (003)

Only scarce information is available regarding thermal experiments on bismuth oxychlorides. Chukhrov et al. (1960) [55] reported a curve for bismoclite which shows characteristic peaks at

625–675 °C and 825–875 °C [4], whereas Rao and Adusumilli (1965) [4] studied a bismoclite sample from Brazil and observed only one endothermic curve between 920 and 930 °C prior to material fusion at 945 °C (Table 7). Despite Rao and Adusumilli (1965) [4] finding no correlation between the data they obtained and those of Chukhrov et al. (1960) [55], the current study has found a clear overlap between 865 and 875 °C (Figure 6). The double endothermic spike is shifted to slightly higher temperatures compared to Chukhrov et al. (1960) [55], possibly due to the effect of trace amounts of preisingerite.

The preparation and photocatalytic activity of BiOCl catalyst was documented recently by Shi et al. (2011) [56]. Their experiment revealed that the TG curve displayed no significant mass loss between 40 and 600 °C, but there was a sharp mass loss after 600 °C with an exothermic peak on the DTA curve, which indicates the point of BiOCl decomposition (Table 7). The DTA curve they obtained had a large endothermic peak below 150 °C, which indicates the evaporation of water molecules and hydrochloric acid. They observed a significant exothermic phenomenon between 600 and 900 °C that might be triggered by a phase change (Table 7). Previous studies have documented the products of thermal decomposition of BiOCl (e.g., $3\text{BiOCl} = \text{Bi}_2\text{O}_3 + \text{BiCl}_3$, a reaction which occurs between 575 and 600 °C; or $\text{Bi}_{24}\text{O}_{31}\text{Cl}_{10}$ ('Arppe compound'), a complex layer structure formed when BiOCl is heated above 600 °C; [57,58]). The thermal experiment carried out in this study identified a constant mass below 600 °C and a sharp mass decrease at higher temperatures. Furthermore, on the DTA curve, spikes below 150 °C and between 600 and 900 °C were recorded. The main difference between this study and that of Shi et al. (2011) [56] is that the exothermic and endothermic spikes are interchanged.

Table 7. Summary of thermal data on BiOCl, Bi₂O₃ and BiAsO₄.

BiOCl	Naturally Occurring BiOCl [55]	Characteristic peak: 625–675 °C Characteristic peak: 825–875 °C
	Naturally occurring BiOCl [4]	Endothermic peak: 920–930 °C Characteristic peak: 945 °C (fusion)
	Synthetic BiOCl [56]	Exothermic peak and sharp mass loss: >600 °C (BiOCl decomposition) Endothermic peak: <150 °C (evaporation of H ₂ O and HCl) Exothermic phenomenon: 600–900 °C (substance transformation)
Bi ₂ O ₃	Synthetic Bi ₂ O ₃ [59]	Characteristic peak: 727 ± 2 °C (α- to δ-Bi ₂ O ₃ transition) Characteristic peak: 822 ± 3 °C (melting point)
BiAsO ₄	Synthetic α-BiAsO ₄ [60]	Characteristic peak: 871 °C (substance transformation)

After the evaporation of HCl and H₂O, the ideal remaining substance is Bi₂O₃. Schröder et al. (2010) [59] verified the temperature range of α- to δ-Bi₂O₃ transitions with in-situ Raman spectroscopy, XRD, DTA and impedance spectroscopy (IS). During the DTA heating process, they only detected one transition from the monoclinic α- to δ-Bi₂O₃ at 727 ± 2 °C before reaching its melting point at 822 ± 3 °C (Table 7). During the cooling process, the δ-phase transformed into tetragonal β-Bi₂O₃ at 639 ± 2 °C and finally back into α-Bi₂O₃ at 563 ± 2 °C. Although not detected in their DTA, the δ-phase sometimes transformed into the cubic γ-phases between 630 and 650 °C, depending on the experimental conditions, and at about 550 °C back into the α-phase. Bi₂O₃ is the ideal heating product after pure bismoclite; none of the DTA spikes and melting point of Bi₂O₃ are analogous to the DTA results of bismoclite from San Francisco de los Andes. This fact is consistent with the presence of trace amounts of preisingerite as indicated by our XRD and chemical analyses. Those features below 250 °C are interpreted as the evaporation of water molecules and hydrochloric acid. The resulting substance is thought to be BiAsO₄ and the peaks between 865 and 893 °C are presumably due to phase changes between the monoclinic α-BiAsO₄ and the tetragonal β-BiAsO₄.

Lee (2008) [60] studied synthetic monoclinic α-BiAsO₄ (rooseveltite) and recorded a phase transformation at 871 °C (Table 7). Her results are consistent with the maximum endothermic peak at 865 °C recorded in our study.

Monoclinic rooseveltite (α-BiAsO₄) has a monazite-like structure. It is dimorphous with tetragonal tetraroseveltite (β-BiAsO₄), which has a scheelite-like structure [61–65]. Monazite and scheelite

structures are adopted by numerous minerals and synthetic compounds including BiAsO₄ and NdAsO₄. Mooney (1948) [62] synthesized bismuth arsenate crystals and noted that the monoclinic form precipitated quickly, whereas the tetragonal form tended to precipitate after a longer period of time. Isostructural compounds such as synthetic NdAsO₄ exhibit a monazite-like structure at room temperature and pressure but have a scheelite-like structure at higher temperature and pressure [66,67]. Finch and Hanchar (2003) [65] published a schematic P–T phase diagram for this group of minerals where monazite-like structure is stable at lower temperatures, making the scheelite-like structure the higher temperature polymorph.

Based on the above discussion, and the consistency with Lee's (2008) [60] DTA results, we consider the endothermic peak at 865 °C (Figure 6) to represent the transition from the monoclinic α -BiAsO₄ (rooseveltite) monzonite-like structure to the tetragonal β -BiAsO₄ (tetrarooseveltite) scheelite-like structure.

Bismoclite is an ionic salt comprising Bi⁺³ cations and O⁻² and Cl⁻ anions. Due to the lack of covalent bonds, most of the absorption features are located in the far infrared region [34]. Bismoclite has two sharp absorptions at approximately 528 and 180 cm⁻¹, as well as two broad absorptions across the ranges 470 to 250 cm⁻¹ and 170 to 85 cm⁻¹ (Table 8) [68]. In the current study, the first absorption peak is consistent with Nyquist et al. (1997) [68]. The second absorption peak could not be fully recorded due to equipment limitations, although Figure 7 shows the beginning of a clear infrared absorption band at wavelength numbers lower than 470 cm⁻¹.

The photocatalytic activity of BiOCl was recently documented by Ye et al. (2012), Bai et al. (2014), Chang et al. (2014), and Xie et al. (2014) [69–72]. By means of FTIR spectroscopy, they recorded the sharpest absorption bands of pure BiOCl at 529, 524, 535 and 523 cm⁻¹, respectively, and a weak peak at approximately 1650 cm⁻¹ (Table 8). Chang et al. (2014) and Xie et al. (2014) [71,72] reported a broad, weak absorption at 3450 cm⁻¹ (Table 8). Ye et al. (2012) [69] and Bai et al. (2014) [70] published IR spectrums up to 2000 cm⁻¹ and documented a minor peak at 1395 cm⁻¹ (Table 8). The main absorption at 528 cm⁻¹, along with the three minor absorption features, were detected in our FTIR study of naturally occurring BiOCl (Figure 7).

The presence of preisingerite at San Francisco de los Andes has been confirmed by means of infrared spectrometry. These results are in agreement with the presence of trace amounts of preisingerite as detected by XRD, geochemistry and DTA. The strong and wide absorption band of OH⁻ group is located in the portion of the electromagnetic spectrum with wavelengths between 4000 and 1700 cm⁻¹. Sejkora et al. (2004) [73] noted that the OH⁻ stretching vibrations of H₂O are located between 2862–3520 cm⁻¹, whereas the δ H₂O bending vibrations occur between 1604 and 1634 cm⁻¹ (Table 8). The last absorption is clearly recorded at 1622 cm⁻¹ (Figure 7).

Sumin de Portilla (1976) [74] studied the nature and role of the hydrogen bonds in legrandite and two other Zn bearing hydroxyl-arsenate minerals. She noted that the (AsO₄)³⁻ ν_3 (T₂), ν_1 (A₁) and ν_4 (T₂) vibration bands are located at around 800, 750 and 400 cm⁻¹, respectively (Table 8). These data are consistent with the sharp spike at 804.76 cm⁻¹, the shoulder detected at 758.05 cm⁻¹, and the beginning of a strong absorption band to the right side of Figure 7. Povarennykh (1978) [75] grouped the characteristic ν_3 and ν_4 vibrations of arsenates between 900–760 cm⁻¹ and 420–310 cm⁻¹ (Table 8). More recent studies documented that the tetrahedral (AsO₄)³⁻ exhibits the ν_1 symmetric stretching vibration (A₁) at 818 cm⁻¹, the ν_3 antisymmetric stretching vibration (F₂) at 786 cm⁻¹, the ν_4 bending vibration (F₂) at 405 cm⁻¹, and the ν_2 symmetric bending vibration (E) at 350 cm⁻¹ (Table 8) [76–79]. The position of IR absorption bands for (AsO₄)³⁻ molecules of preisingerite from San Francisco de los Andes are in agreement with the studies cited above; the main difference between them is the interpretation of absorption peaks.

The stretching vibrations of Bi–O and Bi–O–Bi polyhedral occur between 370 and 620 cm⁻¹ (Table 8) [73,80–82]. These vibrations partially overlap with the main absorptions of bismoclite at 528 cm⁻¹ and the beginning of a broad absorption band at 470 cm⁻¹, as well as with the ν_4 bending vibration of (AsO₄)³⁻ at 405 cm⁻¹.

Fu et al. (2003) [83] noted that the Cl–O stretching vibrations can also be observed at wavelengths above 800 cm^{-1} (Table 8). The absorption at 804 cm^{-1} in Figure 7, can be considered as an overlap of $(\text{AsO}_4)^{3-}$ and Cl–O vibrations of different bonds. The double shoulders at 1392 and 1458 cm^{-1} , as well as the minor inflexion close to 3000 cm^{-1} , are the three major peaks of Nujol (Table 8) [74,84]. Due to a scarcity of references to compare with both Bi-bearing minerals, the double peak at 1092 and 1026 cm^{-1} (Figure 7) could not be clearly attributed to any specific bond, and the origins of these peaks remain unclear.

5.2. Bismoclite from San Francisco de los Andes: Its Genesis and Related Supergene Processes

Bismoclite is insoluble and thus may occur as a dominant phase in the oxidized zones of Bi-rich ore deposits. It has proven to be a key mineral, intimately associated with ores in certain deposits, which includes the Diablillos high-sulfidation epithermal Ag–Au deposit in Argentina. Here, bismoclite is commonly associated with the highest silver grades in the oxide zone [15]. The semi-arid climate favored weathering and supergene enrichment processes, which concentrated native gold and silver minerals. The later occur as chlorargyrite (AgCl), and locally iodargyrite (AgI) [15]. The climate at San Francisco de los Andes is mostly desert with little precipitation, which enabled the occurrence of water-soluble species at surface (e.g., chalcantite) together with bismoclite. The presence of bismoclite (\pm preisingerite) at surface is, therefore, an indicator for areas where supergene and hypogene ores may be found at depth. At San Francisco de los Andes, Cu–sulfates locally can be distinguished at surface due to their brighter colors. However, in areas with higher average rainfall, bismoclite may be the only oxidized mineral present to suggest the presence of hypogene mineralization at depth.

Natural bismoclite typically occurs as small aggregates. Bismoclite from the Diablillos deposit occurs as small masses and fracture coatings, with some aggregates visible in hand specimens [15]. It is commonly intergrown with chlorargyrite in the high-grade silver zones. It is inferred that bismuth at the Diablillos deposit was probably abundant in the hypogene hydrothermal fluids although bismuth minerals (i.e., bismuthinite, matildite) are rare in the preserved hypogene zone [15]. At San Francisco de los Andes, bismoclite forms larger aggregates, some of them up to 3 cm size. In the study area, the bismuth-bearing hypogene mineralogy is evident with particular abundance of bismuthinite and cosalite.

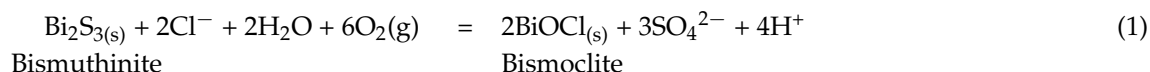
As summarized in Table 1, bismoclite has been documented in the oxidized zones of pegmatites, greisens, W–Mo–(Bi) quartz veins, high-, intermediate-, and low-sulfidation epithermal systems, polymetallic, orogenic, sediment-hosted, volcanogenic massive sulfides, banded iron formations and orthomagmatic Ni–Cu–Fe deposits, but not in porphyries or related magmatic–hydrothermal breccias. When considering element mobility and zoning patterns in mineralized porphyry systems, elements such as Bi, Sb, As, Te, Ag, Pb and Zn are typically anomalously high lateral to the ore zones and/or above them (e.g., Govett, 1983 [85]). They are particularly characteristic in the outer propylitic alteration zones of porphyry deposits and are concentrated at shallow levels in high-, and low-sulfidation epithermal deposits. All the aforementioned elements are characteristic in most of the hypogene S-rich mineral phases that occur as cement in the San Francisco de los Andes breccia pipe complex (Table 2).

Magmatic–hydrothermal breccia systems commonly occur at the apices of porphyry deposits, and often host large amounts of economic mineralization; these ore phases are consistent with those of porphyry-style mineralization (e.g., chalcopyrite, bornite and molybdenite at the Rio Blanco–Los Bronces district, [86]). At the San Francisco de los Andes breccia complex, the characteristic breccia facies and their morphology resemble those of magmatic–hydrothermal breccias in porphyry systems, but are cemented by minerals species more common to distal porphyry and/or shallow epithermal levels.

The rarity of abundant Bi-bearing mineral phases in porphyry and magmatic–hydrothermal breccia deposits is the main reason why bismoclite (and associated preisingerite) have not previously

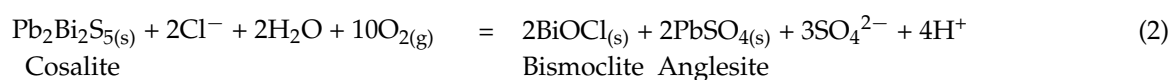
been reported from these types of deposits. For bismoclite to form, it would require available hypogene bismuth minerals; followed by suitable supergene conditions to allow its formation.

In the oxidized zone of San Francisco de los Andes, bismuthinite can be oxidized to bismoclite due to an increase in both Eh and HCl fugacity; e.g.:



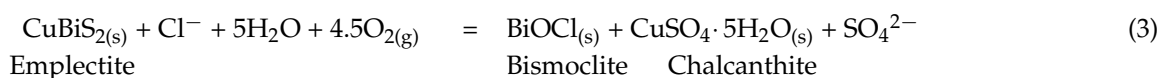
Although it is possible that bismoclite from San Francisco de los Andes may have also formed from Pb–Bi sulfosalt cosalite ($\text{Pb}_2\text{Bi}_2\text{S}_5$) or Cu–Bi sulfosalts such as emplectite (CuBiS_2) and cuprobismutite ($\text{Cu}_{10}\text{Bi}_{12}\text{S}_{23}$), several lines of evidence support bismuthinite as the precursor for bismoclite:

Cosalite is probably the second most abundant hypogene Bi mineral after bismuthinite. Lead is an immobile element in an oxidized and acidic environment such as the San Francisco de los Andes' sulfate-rich oxidized and mixed zones [87,88]. If cosalite was responsible for bismoclite formation, we would expect to find anglesite (PbSO_4) intergrown with the oxychloride as a product; e.g.:



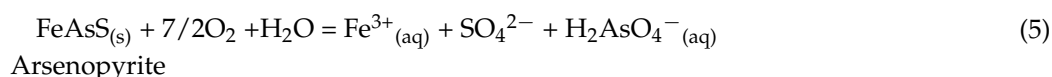
At San Francisco de los Andes, cosalite is unlikely to have been responsible for bismoclite formation because anglesite was only rarely found associated with galena and never with bismoclite.

The only two Cu–Bi sulfosalts found at San Francisco de los Andes are emplectite and cuprobismutite. Either of these hypogene minerals could be responsible for the production of bismoclite, together with the very common chalcantite ($\text{CuSO}_4 \cdot 5\text{H}_2\text{O}$) or less common brochantite ($\text{Cu}_4(\text{SO}_4)(\text{OH})_6$); e.g.:



Emplectite and cuprobismutite are unlikely to have been the hypogene reactants responsible for the formation of bismoclite, as these are minor to rare minerals at San Francisco de los Andes. Furthermore, Cu sulfates were never found in association with bismoclite.

For all of the above, Equation (1) is considered to be the reaction that best describes the formation of bismoclite at San Francisco de los Andes. The sulfate anions liberated from this reaction mostly precipitated as sulfate minerals (Table 2). These, together with arsenates, are the most common supergene mineral groups in the San Francisco de los Andes' oxidized (and to a lesser extent mixed) zones. In a similar manner to bismuthinite, the sulfides and sulfosalts listed in Table 2 most likely reacted with acidic and oxidized meteoric waters to produce additional sulfate anions. Due to the abundance of arsenopyrite at San Francisco de los Andes, a key supergene reaction was the decomposition of arsenopyrite; e.g.:



Arsenic speciation after arsenopyrite decomposition depends on many factors, including pH, oxygen availability, presence of bacteria, and/or Fe^{3+} in solution. In strongly oxidized and moderately acidic conditions, such as the San Francisco de los Andes oxidized zone, the As species produced is predicted to be dihydrogen arsenate [87,89,90]. This anion is most likely responsible for the formation of supergene preisingerite and the abundant Bi, Cu, Pb and Fe arsenates listed in Table 2.

In summary, hypogene S-rich minerals from San Francisco de los Andes were weathered under desert conditions by O₂-rich waters, to produce solutions that dissolved further reduced mineral phases. Hypogene sulfides and sulfosalts were oxidized at the surface and produced sulfuric acid. These reactions led to acidified meteoric waters, which leached metals as they percolated through the oxidized and mixed zones. Above the water table, bismoclite, oxides, arsenates, sulfates and trace carbonates formed; whereas below it, reduced conditions prevailed and hypogene sulfides and sulfosalts remained unaltered. As the supergene solutions penetrated the water table, their metallic content precipitated as secondary reduced species to form the supergene enriched ores. Hypogene iron sulfides reacted with the copper sulfate solution, prompting supergene Cu sulfides and sulfosalt precipitation (i.e., covellite, chalcocite and luzonite) and releasing iron into solution.

Several lines of evidence suggest that bismoclite from San Francisco de los Andes formed due to weathering of bismuthinite by oxidized and moderately acidic fluids. Bismoclite is predicted to form in the supergene environment wherever bismuthinite is exposed to oxygenated saline meteoric waters. Evaporative conditions led to the formation of Cl-bearing minerals, as wet climates preclude their formation.

6. Conclusions

This study provides a detailed account on the origin and mode of formation of rare supergene Bi-minerals, bismoclite and preisingerite at the San Francisco de los Andes breccia complex, which shares many characteristics of magmatic–hydrothermal breccias recognized in porphyry systems. Our new data deliver an up to date comparison to the limited published data on naturally occurring bismoclite–preisingerite, and their synthetic equivalents. Furthermore, previous studies on these species have not always yielded consistent results.

This article documents the first occurrence of bismoclite in a porphyry-related, magmatic–hydrothermal breccia-hosted deposit. This bismuth oxyhalide was found within the oxidized zone at San Francisco de los Andes tourmaline–cemented breccia pipe. Hypogene bismuthinite (and less likely Bi sulfosalts) cementing breccia fragments weathered to bismoclite due to their interaction with saline meteoric waters under high Eh and moderately low pH conditions.

Bismoclite is an insoluble mineral that occurs as a minor or trace phase in a wide variety of Bi-bearing ore deposit types. When bismoclite occurs as a major mineral in the oxidized zone of weathered deposits, it is a diagnostic mineral that may indicate the presence of hypogene and supergene Bi mineralization (and associated metals) at depth. The detection of bismoclite is of particular importance in mineral exploration in those areas where the supergene profile has been leached to remove the presence of characteristic, water-soluble indicator minerals at the surface (e.g., Cu sulfates). Whereas Fe-oxides and hydroxides can also indicate the potential presence of hypogene mineralization, they can equally reflect areas formed by the oxidation of pyrite alone.

Bismoclite has been documented in the oxidized zone of numerous Bi-bearing ore deposit types, but never in Cu–Mo porphyry deposits, or related magmatic–hydrothermal breccias. The San Francisco de los Andes breccia complex shows similar geometry, morphology and internal organization as those found in traditional magmatic–hydrothermal breccias associated with Cu–Mo porphyry deposits, although it is cemented by minerals rich in Bi, Sb, As, Te, Ag, Pb and Zn. These elements tend to be anomalously high in the outer propylitic alteration zones (laterally or above the ore zones in porphyry systems), but rarely are abundant enough to form dominant hypogene minerals to cement magmatic–hydrothermal breccias. For bismoclite (and associated preisingerite) to form requires the presence of hypogene Bi-bearing minerals followed by appropriate supergene conditions. These hypogene minerals commonly occur only as trace phases, or are entirely absent, in porphyry and related magmatic–hydrothermal breccia deposits. The scarcity of hypogene Bi-mineral phases in porphyry and related magmatic–hydrothermal breccia deposits is the main reason why bismoclite has not previously been reported in these types of deposits.

Acknowledgments: This work was done as part of a Ph.D. thesis supported by the University of Tasmania (Australia) and Universidad Nacional del Sur (Argentina). A scholarship was provided by AMIRA P1060 (Australia), the ARC Research Hub for Transforming the Mining Value Chain (project number IH130200004, Australia) and CONICET (Argentina). The main author is grateful to Edward M. Suzuki from the Seattle Crime Laboratory Division, Washington State Patrol and Olga I. Pieroni from the Chemistry Department, Universidad Nacional del Sur for their generous help and invaluable advices concerning IR analyses. A special thanks is also extended to David Hutchinson for reading the original manuscript and providing relevant suggestions about the scientific content and reasoning, as well as editorial assistance. Last but not least, we gratefully acknowledge the two anonymous reviewers selected by Minerals who examined the original manuscript; their critical reading and valuable comments greatly improved this article.

Author Contributions: This article represents a joint effort from the team of authors. Francisco J. Testa analyzed the bismoclite samples, interpreted the results and wrote the manuscript. David R. Cooke and Lejun Zhang were involved during the interpretation of the data and provided valuable ideas for the discussion, as well as edited the entire manuscript. Graciela R. Mas, along with Francisco J. Testa, conducted the fieldwork, sample collection and the X-ray analysis and interpretation.

Conflicts of Interest: The authors declare no conflict of interest. The founding sponsors had no role in the design of the study; in the collection, analyses, or interpretation of data; in the writing of the manuscript, and in the decision to publish the results.

References

1. Mountain, E.D. Two new bismuth minerals from South Africa. *Mineral. Mag.* **1935**, *24*, 59–64. [[CrossRef](#)]
2. Bedlivi, D.; Mereiter, K. Preisingerite, $\text{Bi}_3\text{O}(\text{OH})(\text{AsO}_4)_2$, a new species from San Juan Province, Argentina: Its description and crystal structure. *Am. Mineral.* **1982**, *67*, 833–840.
3. Färber, G.; Witzke, T. Exotische Pseudomorphosen aus Brasilien: Waylandit nach Wismutglanz. *Lapis* **2011**, *36*, 42–43. (In German)
4. Rao, A.B.; Adusumilli, M.S. Bismoclite from Brazil. *Can. Mineral.* **1965**, *8*, 390–391.
5. Billows, E. *I minerali della Sardegna ed i loro giacimenti*; Sardegna Mineraria, Istituto per gli studi Sardi, Regia Università di Cagliari: Cagliari, Italy, 1941. (In Italian)
6. Kristiansen, R. Nye mineralfunn i Norge. *Stein* **2008**, *35*, 17–21. (In Norwegian)
7. Anthony, J.W.; Bideaux, R.A.; Bladh, K.W.; Nichols, M.C. Handbook of Mineralogy. *Mineral. Soc. Am.* **1997**, *3*, 61.
8. Sharpe, J.L.; Williams, P.A. Secondary bismuth and molybdenum minerals from Kingsgate, New England district of New South Wales. *Aust. J. Mineral.* **2004**, *10*, 7–12.
9. Von Bezings, L.; Bode, R.; Jahn, S. *Namibia Minerals and Localities*; Bode Verlag GmbH: Salzhemmendorf, Germany, 2007; p. 411.
10. Ellingsen, H.V.; Andersen, T.; Haugen, A. Nye mineraler fra amazonitt pegmatitten ved Tennvatn, Nordland. *Norsk Bergverksmus. Skr.* **2000**, *17*, 52–58. (In Norwegian)
11. Frondel, C. New data on agricolite, bismoclite, koechlinite and the bismuth arsenates. *Am. Mineral.* **1943**, *28*, 536–540.
12. Evseev, A.A. Kazakhstan and Middle Asia. A Brief Mineralogical Guide. *World Stones* **1995**, *8*, 24–30.
13. Walenta, K. Die Mineralien des Schwarzwaldes und ihre Fundstellen. Weise, Ch: Munich, Germany, 1992; p. 336. (In German)
14. Birch, W.D.; Grey, I.E.; Mills, S.J.; Bougerol, C.; Pring, A.; Ansermet, S. Pittongite, a new secondary tungstate from Pittong, Victoria, Australia. *Can. Mineral.* **2007**, *45*, 857–864. [[CrossRef](#)]
15. Stein, D.M. The Diablillos Ag–Au Deposit, Salta, Argentina: Deeply oxidized high–sulphidation epithermal mineralization in the Southern Puna Province. Master’s Thesis, Queen’s University, Kingston, ON, Canada, 2001; p. 151.
16. Schaller, W.T. Bismoclite from Goldfield, Nevada. *Am. Mineral.* **1941**, *26*, 651–654.
17. De Graaf, M.L.D. Kudriavvy Volcano. Mineralogy of Russia 2009. Available online: <http://maurice.strahlen.org/kurilles/kurilles.htm> (accessed on 24 June 2016).
18. Campostrini, I.; Demartin, F.; Gramaccioli, C.M. Vulcano: Ein außergewöhnlicher Fundpunkt von neuen und seltenen Mineralien. *Mineralien-Welt* **2010**, *21*, 40–57. (In German)
19. Zelenski, M.; Bortnikova, S. Sublimate speciation at Mutnovsky volcano, Kamchatka. *Eur. J. Mineral.* **2005**, *17*, 107–118. [[CrossRef](#)]

20. Foord, E.E.; Shawe, D.R.; Conklin, N.M. Coexisting galena, PbS₂₂ and sulfosalts; evidence for multiple episodes of mineralization in the Round Mountain and Manhattan gold districts, Nevada. *Can. Mineral.* **1988**, *26*, 355–376.
21. Marinelli, G.I. Minerali di bismuto del cantiere Falcacci a Rio Marina, Isola d'Elba. *Atti Soc. Toscana Sci. Nat.* **1959**, *66*, 337–352. (In Italian)
22. Senesi, F.; Hanauer, M.; Rogner, P.I. Minerali di bismuto di Rio Marina, Isola d'Elba. *Riv. Mineral. Ital.* **2013**, *4*, 234–242. (In Italian)
23. Ahlfeld, F. *Los Yacimientos Minerales de Bolivia*; Imprenta Industrial S.A.: Bilbao, Spain, 1954; p. 277. (In Spanish)
24. Tindle, A.G. *Minerals of Britian and Ireland*; Terra Publishing: Harpenden, UK, 2008; p. 616.
25. Adams, P. The Brown Monster and Reward Mines Inyo County, California. *Mineral. Rec.* **2010**, *41*, 175–193.
26. Means, A.H. Some new mineral occurrences from the Tintic District, Utah. *Am. J. Sci.* **1916**, *41*, 125–130. [[CrossRef](#)]
27. Ii and Hori. Koubutsu–Gakkai Kou'en–Youshi, Japan, 1992, p. 159.
28. Tormanen, T.O.; Koski, R.A. *Bismuth and Gold Mineralogy of Pyrrhotite-rich Massive Sulfide Deposits from the Escanaba Trough, Southern Gorda Ridge*; Eos, Transactions American Geophysical Union, 81, Fall Meeting Supplement; AGU Publications: Washington, DC, USA, 2000.
29. Pring, A.; Francis, G.; Birch, W.D. Nissonite, namibite, and other additions to the mineral suite from Iron Monarch, South Australia. *Aust. Miner.* **1992**, *6*, 31–39.
30. Li, C.; Naldrett, A.J. Platinum–group minerals from the Deep Copper zone of the Strathcona deposit, Sudbury, Ontario. *Can. Mineral.* **1993**, *31*, 31–44.
31. Plust, H.G. *Process for the Preparation of Pure Bismuth*; United States Patent Office, United States of America: Alexandria, VA, USA, 1965.
32. Rieger, C.J. Pearlescent pigments. In *Paint and Coating Testing Manual*; Koleske, J.V., Ed.; ASTM International—American Society for Testing & Materials: West Conshohocken, PA, USA, 1995; pp. 229–237.
33. Novinski, S.J.; Noak, P.; Venturini, M. Employing pearlescent pigments in high-performance coatings. *Paint Coat. Ind.* **1998**, *14*, 62–68.
34. Suzuki, E.M. Infrared Spectra of U.S. Automobile Original Finishes (1998–2000). IX. Identification of Bismuth Oxychloride and Silver/White Mica Pearlescent Pigments Using Extended Range FT–IR Spectroscopy, XRF Spectrometry, and SEM/EDS Analysis. *J. Forensic Sci.* **2014**, *59*, 1205–1225. [[CrossRef](#)] [[PubMed](#)]
35. Suzuki, E.M. *Identification of Bismuth Oxychloride, a Pearlescent Pigment, in Automotive Paint Using Infrared Spectroscopy and Elemental Analysis*; PPT Presentation: Seattle, WA, USA, 2011.
36. Cardó, R.; Segal, S.; Korzeniewski, L.I.; Palacio, M.B.; Chernicoff, C. Estudio Metalogenético de brechas hidrotermales portadoras de mineralización de Bi–Au–Cu en el ámbito de Cordillera Frontal, provincia de San Juan. In *Serie Contribuciones Técnicas, Recursos Minerales N° 31*; Servicio Geológico Minero Argentino, SEGEMAR: Buenos Aires, Argentine Republic, 2008; pp. 2–28. (In Spanish)
37. Llambías, E.J.; Malvicini, L. The geology and genesis of the Bi–Cu mineralized breccia–pipe, San Francisco de los Andes, San Juan, Argentina. *Econ. Geol.* **1969**, *64*, 271–286. [[CrossRef](#)]
38. Ramos, V.A. The tectonic of the Central Andes: 30° to 33° S latitude. In *Processes in Continental Lithospheric Deformation*; Clark, S., Burchfiel, D., Eds.; Geological Society of America: Boulder, CO, USA, 1988; pp. 31–54.
39. Busquets, P.; Colombo Piñol, F.; Solé de Porta, N.; Heredia Carballo, N.; Rodríguez Fernández, L.R.; Álvarez Marrón, J. Carbonífero superior en la Cordillera Frontal (Provincia de San Juan, Argentina): Características e implicaciones regionales. *Geogaceta* **2002**, *32*, 251–254. (In Spanish)
40. Rodríguez Fernández, L.R.; Heredia, N.; Gallastegui, G.; Busquets, P.; Colombo, F. The Argentine Frontal Cordillera between 30°00' and 31°30' S latitude: Polycyclic structure and tectonic evolution. *Geogaceta* **2002**, *32*, 167–170.
41. Rodríguez Fernández, L.R.; Heredia, N.; Gallastegui, G.; Quesada, C.; Robador, A.; Marín, G.; Cardó, D.R. *Texto explicativo de la Carta Geológica No 3169-14 a escala 1:100.000 (Paraje de Castaño Viejo)*; Instituto de Geología y Recursos Minerales, Servicio Geológico Minero Argentino (SEGEMAR): Buenos Aires, Argentina, 1996; p. 145. (In Spanish)
42. Nasi, C.P.; Mpodozis, C.M.; Cornejo, P.P.; Moscoso, R.D.; Maksae, V.J. El batolito Elqui–Limarí (Paleozoico Superior–Triásico): Características petrográficas, geoquímicas y significado tectónico. *Rev. Geol. Chile* **1985**, *25–26*, 77–111. (In Spanish)

43. Ramos, V.A.; Jordan, T.A.; Allmendinger, R.W.; Mpodozis, S.; Kay, S.M.; Cortes, J.M.; Palma, M.A. Paleozoic terranes of the central Argentine–Chilean Andes. *Tectonics* **1986**, *5*, 855–880. [[CrossRef](#)]
44. Kay, S.M.; Ramos, V.A.; Mpodozis, C.; Sruoga, P. Late Paleozoic to Jurassic silicic magmatism at the Gondwana margin: Analogy to the Middle Proterozoic in North America? *Geology* **1989**, *17*, 324–328. [[CrossRef](#)]
45. Llambías, E.J.; Sato, A.M. El batolito de Colangüil: Transición entre orogénesis y anorogénesis. *Rev. Asoc. Geol. Argent.* **1995**, *50*, 111–131. (In Spanish)
46. Llambías, E.J.; Sato, A.M. El batolito de Colangüil (29–31° S) Cordillera Frontal de Argentina: Estructura y marco tectónico. *Rev. Geol. Chile* **1990**, *17*, 89–108. (In Spanish)
47. Lencinas, A.N. *Informe sobre Mina San Francisco de los Andes*; Compañía Minera Aguilar S.A.: El Aguilar, Argentina, 1990. (In Spanish)
48. Angelelli, V. *Yacimientos Metalíferos de la República Argentina. Volumen 1. Comisión de Investigaciones Científicas de la provincia de Buenos Aires, Facultad de Ciencias Naturales y Museo de La Plata—UNLP; Instituto de Geología Aplicada: Almadén, Spain, 1984; p. 382.* (In Spanish)
49. Bedlivy, D.; Llambías, E.J. Arseniatos de Cu, de Fe, y de Pb de San Francisco de los Andes, Provincia de San Juan, Republica Argentina. *Rev. Asoc. Geol. Argent.* **1969**, *24*, 29–40. (In Spanish)
50. Bannister, F.A.; Hey, M.H. Crystal structure of the bismuth oxyhalides. *Nature* **1934**, *134*, 856–857. [[CrossRef](#)]
51. Bannister, F.A.; Hey, M.H. The crystal structure of the bismuth oxyhalides. *Mineral. Mag.* **1935**, *24*, 49–58. [[CrossRef](#)]
52. Keramidas, K.G.; Voutsas, G.P.; Rentzeperis, P.I. The crystal structure of BiOCl. *Z. Kristallogr.* **1993**, *205*, 35–40.
53. Ketterer, J.; Krämer, V. Structure refinement of bismuth oxide bromide, BiOBr. *Acta Crystallogr.* **1986**, *C42*, 1098–1099. [[CrossRef](#)]
54. Singh, A.K. *Advanced X-ray Techniques in Research and Industry*; IOS Press: Amsterdam, The Netherlands, 2005.
55. Chukhrov, Senderova and Ermilova. Cit. Skifax D.T.A. Index. 1960. In Rao, A.B.; Adusumilli, M.S. Bismoclite from Brazil. *Can. Mineral.* **1965**, *8*, 390–391.
56. Shi, Z.; Wang, Y.; Fan, C.; Wang, Y.; Ding, G. Preparation and photocatalytic activity of BiOCl catalyst. *Trans. Nonferrous Met. Soc. China* **2011**, *21*, 2254–2258. [[CrossRef](#)]
57. Greenwood, N.N.; Earnshaw, A. *Chemistry of the Elements*, 2nd ed.; Butterworth-Heinemann: Oxford, UK, 1997; p. 572.
58. Eggenweiler, U.; Keller, E.; Krämer, V. Redetermination of the crystal structures of the ‘Arppe compound’ Bi₂₄O₃₁Cl₁₀ and the isomorphous Bi₂₄O₃₁Br₁₀. *Acta Crystallogr. Sect. B Struct. Sci.* **2000**, *B56*, 431–437. [[CrossRef](#)]
59. Schröder, F.; Bagdassarov, N.; Ritter, F.; Bayarjargal, L. Temperature dependence of Bi₂O₃ structural parameters close to the α – δ phase transition. *Phase Transit.* **2010**, *83*, 311–325. [[CrossRef](#)]
60. Lee, S.L. *Fluorite Type Oxide Ion Conductors of Bi₂O₃-M₂O₅ (M = P, As, V)*; Ibnu Sina Institute for Fundamental Science Studies, Universiti Teknologi Malaysia: Johor Bahru, Malaysia, 2008; p. 216.
61. Herzenberg, R. Nuevos minerales de Bolivia. In *Boletín Técnico N 1. Facultad Nacional de Ingeniería*; Universidad Técnica de Oruro: Oruro, Bolivia, 1946. (In Spanish)
62. Mooney, R.C.L. Crystal structure of tetragonal bismuth arsenate, BiAsO₄. *Acta Crystallogr.* **1948**, *1*, 163–165. [[CrossRef](#)]
63. Schwarz, V.H. Die phosphate, arsenate und vanadate der Seltenen erden. *Z. Anorg. Allg. Chem.* **1963**, *323*, 44–56. (In German) [[CrossRef](#)]
64. Sejkora, J.; Řídkošil, T. Tetraaroseveltite, β -Bi(AsO₄), a new mineral species from Moldava deposit, the Krušné hory Mts., Northwestern Bohemia, Czech Republic. In *Neues Jahrbuch für Mineralogie, Monatshefte*; E. Schweizerbart'sche Verlagsbuchhandlung: Stuttgart, Germany, 1994; pp. 179–184.
65. Finch, R.J.; Hanchar, J.M. *Structure and Chemistry of Zircon and Zircon-Group Minerals*; Hanchar, J.M., Hoskin, P.W.O., Eds.; Reviews in Mineralogy and Geochemistry; Mineralogical Society of America: Chantilly, VA, USA, 2003; Volume 53, pp. 1–26.
66. Stubican, V.S.; Roy, R. High-pressure scheelite-structure polymorphs of rare-earth vanadates and arsenates. *Z. Krist.* **1963**, *119*, 90–97. [[CrossRef](#)]
67. Mazhenov, N.A.; Nurgaliev, B.Z.; Muldakhmetov, K.Z. Scheelite modification of neodymium arsenate. *Inorg. Mater.* **1988**, *24*, 991–993.
68. Nyquist, R.A.; Putzig, C.L.; Kagel, R.O. *The Handbook of Infrared and Raman Spectra of Inorganic Compounds and Organic Salts*; Academic Press: Cambridge, MA, USA, 1997; p. 224.

69. Ye, L.; Gong, C.; Liu, J.; Tian, L.; Peng, T.; Dengb, K.; Zan, L. $\text{Bi}_n(\text{Tu})_x\text{Cl}_{3n}$: A novel sensitizer and its enhancement of BiOCl nanosheets' photocatalytic activity. *J. Mater. Chem.* **2012**, *22*, 8354–8360. [[CrossRef](#)]
70. Bai, Y.; Wang, P.-Q.; Liu, J.-Y.; Liu, X.-J. Enhanced photocatalytic performance of direct Z-scheme BiOCl-g-C₃N₄ photocatalysts. *RSC Adv.* **2014**, *4*, 19456–19461. [[CrossRef](#)]
71. Chang, F.; Xie, Y.; Zhang, J.; Chen, J.; Li, C.; Wang, J.; Luo, J.; Denga, B.; Hu, X. Construction of exfoliated g-C₃N₄ nanosheets–BiOCl hybrids with enhanced photocatalytic performance. *RSC Adv.* **2014**, *4*, 28519–28528. [[CrossRef](#)]
72. Xie, T.; Xu, L.; Liu, C.; Yang, J.; Wang, M. Magnetic composite BiOCl-SrFe₁₂O₁₉: A novel p–n type heterojunction with enhanced photocatalytic activity. *Dalton Trans.* **2014**, *43*, 2211–2220. [[CrossRef](#)] [[PubMed](#)]
73. Sejkora, J.; Cejka, J.; Hlousek, J.; Novak, M.; Srein, V. Phosphowalpurkite, The (PO₄)[−] Dominant Analogue of Walpurgite, from Smrkovec, Slavkovsky Les Mountains, Czech Republic. *Can. Mineral.* **2004**, *42*, 963–972. [[CrossRef](#)]
74. De Sumin Portilla, V.I. The nature of hydrogen bonds and water in legrandite by IR spectroscopy. *Am. Mineral.* **1976**, *61*, 95–99.
75. Povarennykh, A.S. The use of infrared spectra for the determination of minerals. *Am. Mineral.* **1978**, *63*, 956–959.
76. Nakamoto, N. *Infrared and Raman Spectra of Inorganic and Coordination Compounds*, 4th ed.; Wiley-Interscience: New York, NY, USA, 1986.
77. Myneni, S.C.B.; Traina, S.J.; Waychunas, G.A.; Logan, T.J. Experimental and Theoretical Vibrational Spectroscopic Evaluation of Arsenate coordination in Aqueous Solutions and Solids. *Geochim. Cosmochim. Acta* **1998**, *62*, 3285–3300. [[CrossRef](#)]
78. Myneni, S.C.B.; Traina, S.J.; Waychunas, G.A.; Logan, T.J. Vibrational spectroscopy of functional group chemistry and arsenate coordination in ettringite. *Geochim. Cosmochim. Acta* **1998**, *62*, 3499–3514. [[CrossRef](#)]
79. Cejka, J.; Sejkora, J.; Plasil, J.; Keeffe, E.C.; Bahfenne, S.; Palmer, S.J.; Frost, R.L. A raman and infrared spectroscopic study of Ca²⁺ dominant members of the mixite group from the Czech Republic. *J. Raman Spectrosc.* **2011**, *42*, 1154–1159. [[CrossRef](#)]
80. Hazra, S.; Mandal, S.; Ghosh, A. Properties of unconventional lithium bismuthate glasses. *Phys. Rev. B* **1997**, *56*, 8021–8025. [[CrossRef](#)]
81. Sreenivasu, D.; Chandramouli, V. EPR, IR and DC conductivity studies of xCuO-(100-x) Bi₂O₃ glasses. *Bull. Mater. Sci.* **2000**, *23*, 281–284. [[CrossRef](#)]
82. Szaller, Z.; Kovacs, L.; Poppl, L. Comparative study of bismuth tellurites by infrared absorption spectroscopy. *J. Solid State Chem.* **2000**, *152*, 392–396. [[CrossRef](#)]
83. Fu, H.; Zhou, Z.; Zhou, X. Hydrogen bonding between chlorine oxide and water (H₂O·ClO) radical complex. *Chem. Phys. Lett.* **2003**, *382*, 466–474. [[CrossRef](#)]
84. Miller, F.A.; Wilkins, C.H. Infrared Spectra and Characteristic Frequencies of Inorganic Ions. *Anal. Chem.* **1952**, *24*, 1253–1294. [[CrossRef](#)]
85. Govett, G.J.S. *Rock Geochemistry in Mineral Exploration—Handbook of Exploration Geochemistry*; Elsevier: New York, NY, USA, 1983; Volume 3, pp. 181–225.
86. Frikken, P.H.; Cooke, D.R.; Walshe, J.L.; Archibald, D.; Skarmeta, J.; Serrano, L.; Vargas, R. Mineralogical and isotopic zonation in the Sur–Sur tourmaline breccia, Río Blanco–Los Bronces Cu–Mo deposit, Chile: Implications for ore genesis. *Econ. Geol.* **2005**, *100*, 935–961. [[CrossRef](#)]
87. Brookins, D.G. *Eh–pH Diagrams for Geochemistry*; Springer Verlag: Berlin, Germany, 1988; p. 176.
88. Pirajno, F. *Hydrothermal Processes and Mineral Systems*; Springer Verlag: Berlin, Germany, 2009; pp. 1–200.
89. Takeno, N. *Atlas of Eh–pH Diagrams—Intercomparison of Thermodynamic Databases*; Geological Survey of Japan Open File Report No. 419; National Institute of Advanced Industrial Science and Technology, Research Center for Deep Geological Environments: Tokyo, Japan, 2005.
90. Lu, P.; Zhu, C. Arsenic Eh–pH diagrams at 25 °C and 1 bar. *Environ. Earth Sci.* **2011**, *62*, 1673–1683. [[CrossRef](#)]

